ORIGINAL ARTICLE

Distal planar rotary scanner for endoscopic optical coherence tomography

Kyle Searles[1] · Nabil Shalabi[2] · Geoffrey Hohert[3] · Nirvana Gharib[2] · Sayed Mohammad Hashem Jayhooni[2] · Pierre M. Lane[3] · Kenichi Takahata[1,2]

Abstract

Optical coherence tomography (OCT) is becoming a more common endoscopic imaging modality for detecting and treating disease given its high resolution and image quality. To use OCT for 3-dimensional imaging of small lumen, embedding an optical scanner at the distal end of an endoscopic probe for circumferential scanning the probing light is a promising way to implement high-quality imaging unachievable with the conventional method of revolving an entire probe. To this end, the present work proposes a hollow and planar micro rotary actuator for its use as an endoscopic distal scanner. A miniaturized design of this ferrofluid-assisted electromagnetic actuator is prototyped to act as a full 360° optical scanner, which is integrated at the tip of a fiber-optic probe together with a gradient-index lens for use with OCT. The scanner is revealed to achieve a notably improved dynamic performance that shows a maximum speed of 6500 rpm, representing 325% of the same reported with the preceding design, while staying below the thermal limit for safe *in-vivo* use. The scanner is demonstrated to perform real-time OCT using human fingers as live tissue samples for the imaging tests. The acquired images display no shadows from the electrical wires to the scanner, given its hollow architecture that allows the probing light to pass through the actuator body, as well as the quality high enough to differentiate the dermis from the epidermis while resolving individual sweat glands, proving the effectiveness of the prototyped scanner design for endoscopic OCT application.

Keywords Optical scanner · Electromagnetic actuator · Ferrofluid · Endoscopic probe · Optical coherence tomography

1 Introduction

Optical coherence tomography (OCT) is increasingly playing an important role in clinical settings given its ability to image high-resolution cross sections of tissue in real time [1–5]. This imaging modality operates by directing low coherence, non-ionizing light onto the area of interest and collecting the backscattered light along the same optical path [2, 5]. While this process is similar to ultrasound imaging, since OCT uses light waves instead of sound waves, it provides much higher resolution [2]. Given its high resolution and non-destructive nature, OCT is widely used for a variety of applications, including those implemented in the form of fiber-optic endoscopes for luminal imaging of, e.g., cardiovascular, gastrointestinal tract, lung, and urinary tract [3]. For example, it is commonly used for cardiovascular assessment of plaque structures in coronary arteries using an OCT probe [1]. To be able to image the inner walls of these narrow ducts, the light beam (typically a near-infrared laser beam for OCT [1–5]) is circumferentially scanned over the lumen wall, which is traditionally achieved by rotating an optical fiber and lens assembly within a stationary window tube. Here, torque from an external (proximal) motor is transmitted to the rotating fiber using a flexible torque coil and a fiber-optic rotary joint [3, 6]. More modern beam rotation techniques involve embedding a micromotor at the tip (distal end) of the probe to rotate an angled mirror (and thus the light beam bent at the mirror surface), which reduces the image distortion known as NURD (non-uniform rotational distortion) seen in devices that use an

✉ Kenichi Takahata
    takahata@ece.ubc.ca

1   School of Biomedical Engineering, University of British Columbia, Vancouver, BC V6T 1Z3, Canada

2   Department of Electrical and Computer Engineering, University of British Columbia, Vancouver, BC V6T 1Z4, Canada

3   Integrative Oncology, BC Cancer Research Institute, Vancouver, BC V5Z 4E6, Canada

external motor and torque coil [1, 3, 6–17]. The same goal has also been approached by developing scanners based on the micro-electro-mechanical systems (MEMS) technology for their distal integration with OCT endoscopes [1, 16, 18–20]. However, these MEMS-based scanners, which actuate suspended planar mirrors for optical scanning, have inherent limitations in their scanning angles (e.g., 28° [19]) due to the 2-dimensional nature of their silicon-based structures. While the OCT endoscope that incorporated a circular array of MEMS scanners was reported to circumvent the scanning range issue and have a full circumferential view [20], the entire scanner unit had to become complex while enlarging the overall scanner size (having an outer diameter of > 10 mm [20]).

Toward realizing miniaturized tip-active side-viewing endoscopes that allow for beam rotation enabling a full 360° imaging, there have been recent studies on the distal scanners using ferrofluid-based electromagnetic micro rotary actuators [21–24]. These actuators are designed to have tubular configurations, in which the rectangular magnet rotor is rotated with the stator coils patterned on the packaging tube. The low-friction bearing of the actuator is achieved by a layer of ferrofluid, a magnetic liquid functionalized by ferromagnetic nanoparticles [25], which is magnetically self-sustained on the rotor. This configuration significantly simplifies the actuator design and in turn contributes to reducing the radial size of the resultant scanner as well as its potential cost (cf., commercial small motors that have been used for the same purpose cost $1000-$2000 per unit [3]). These scanners are capable of multimodal (high-speed and stepping) operation, allowing for the use of different imaging techniques such as OCT and Raman spectroscopy with the side-viewing endoscopes [21–24]. However, given their tubular nature, they suffer from having a relatively large axial size (~ 5 mm), which reduces the flexibility of the endoscope's distal portion in which they are embedded. They are also not hollow, i.e., the mirror must face the proximal end of the endoscope, which causes shadows to be produced by the electrical wiring used to power the scanners [21–24].

The objectives of this work are to investigate and develop a new design of the ferrofluid-based distal micro actuator/scanner based on a planar architecture that enables a shadowless full circumferential scan, and experimentally demonstrates its endoscopic OCT imaging application through high-speed (several 1000's rpm) scanning rates for the first time. This planar-form actuator electromagnetically spins a ferrofluid-applied magnet rotor using a printed flat stator, both of which are closely aligned perpendicular to the optical axis of the endoscopic probe and packaged with a prism mirror to be revolved at the probe tip within the scanner housing. Both the rotor and the stator have ring-shaped structures so that the entire scanner has a hollow

construction [26]. This hollow design provides an optical path for a probing light to travel through the actuator and be bent at the revolving prism mirror located at the most distal end of the probe, which ensures that the power leads do not block the imaging light (as in other distal scanners [12, 15]) and thus gives a 360° field of view image. This planar scanner is integrated at the tip of a fiber-optic probe coupled with an OCT system to shows its viability as an endoscopic distal scanner (Fig. 1). The design and prototyping of this new scanner are described in the next section. This is followed by experimental results that characterize the new actuator's performance and demonstrate its unobstructed OCT imaging ability.

2 Materials and methods

2.1 Device design and drive principle

The first planar hollow actuator used in the distal scanner was developed as a proof of concept to verify the actuator's fundamental ability to rotate a laser beam in an unobstructed fashion [26] (this particular actuator architecture is referred to as the *test* design in this work). This test design is newly
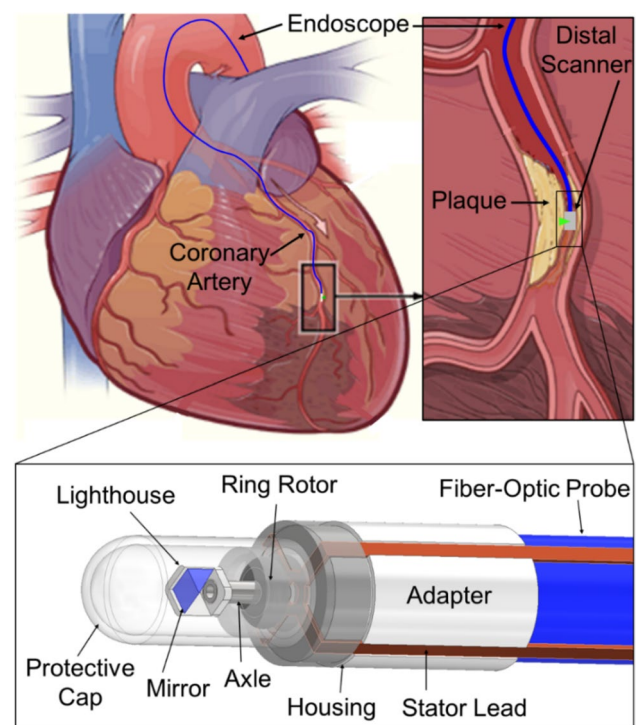
Fig. 1 Conceptual diagram of the actuator used as a distal scanner in an optical coherence tomography endoscope for plaque assessment in the coronary arteries (heart image sourced from the website of the National Institutes of Health (www.nhlbi.nih.gov/health/heart-attack/causes) and modified)

enhanced to adapt it to an OCT system for imaging with an improved scanning performance. The new actuator design is composed of a rotor, housing, and stator (Fig. 2a). The rotor is a diametrically polarized ring magnet with a hollow axle, and a 45° prism mirror secured in its holder (called "lighthouse" in this work) is attached to the top. The magnet is uniformly covered by ferrofluid to act as a liquid-phase bearing that minimizes friction and allows smooth rotation [21–24]. To generate the magnetic fields that rotate the magnet, a stator is placed behind the magnet. The stator is a copper circle that is photo-patterned onto polyimide film, where a digital voltage (high or low) is applied at each of the four leads to generate one of two lateral magnetic flux shapes, diagonal and parallel (Fig. 2b), on the plane where the rotor is located [26]. The diametrically polarized rotor is consequently aligned to a specific orientation of the produced field. The above two voltage configurations are symmetrically patterned around the stator to form eight unique steps which can be cycled at a high speed to obtain continuous rotation. The rotor and stator are all assembled into a 3D-printed housing to package the scanner device and its adapter to fiber optics (Fig. 2a).
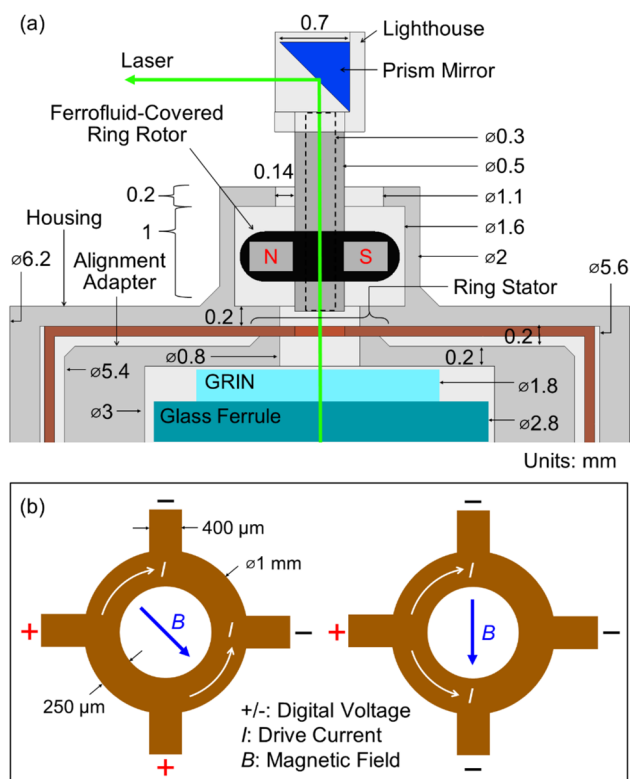
Fig. 2 New device design. **a** Cross-sectional schematic of the developed distal scanner (protective tube not illustrated) with the alignment adapter used for high-precision optical connection with the OCT probe. **b** The ring stator of the actuator showing (left) one of four diagonal-field powering configurations and (right) one of four parallel-field current configurations

The scanner design is further miniaturized from the test design by structurally modifying both the housing and rotor while leveraging the proven stator design and drive mechanism. The housing is axially shrunk by 64% (from 5 mm to 1.8 mm) to match the working distance of the gradient-index (GRIN) lens, ensuring in-focus OCT imaging with the integrated fiber-optic probe. This axial shrinkage accordingly shortens the rigid portion at the distal end of the probe, helping increase its flexibility and maneuverability in curvy small lumen (and thus minimize a possibility of tissue damage). An off-center top cap is added to prevent the rotor component from coming off its original position as the device is tilted during use. The cap being off-center allows the component to be easily assembled without ferrofluid, and when ferrofluid is added to the rotor, the surface tension centers it within the housing, so that the rotor can no longer pass through the off-centered hole to be secured inside the housing under any tilted position. The prism mirror was placed upside down in the lighthouse so that the laser beam was bent on its angled mirror surface in air (instead of the back of the mirror in the glass, the case of the test design [26]) in order to avoid any attenuation of the OCT beam so as to improve the image quality.

A key difference between the new and test designs is the distance between the magnet and the stator, which is reduced to 20% of the test design (0.45 mm vs. 2.25 mm, assuming a ferrofluid thickness of 250 μm for both). This reduction of the particular separation leads directly to an increase in the field strength, B, that the magnet rotor is exposed to, which is given by:

$$B = \mu_0 \cdot I/(2\pi \cdot d) \tag{1}$$

where μ_0 is the permeability of free space, I is the current, and d is the distance from the wire. A finite element analysis was conducted (using COMSOL® version 5.6) to evaluate the magnetic flux density at various distances from the center of the stator. The simulation results followed the theory of a current carrying wire, with the magnetic field strength being inversely proportional to the distance from the stator, as shown in Fig. 3. By looking at each design's rotor–stator distance (indicated in Fig. 3), it was found that the field intensity in the new design was ~2.9× greater for both the parallel and diagonal powering modes compared with the test design (Table 1). This also means that the drive current can be reduced by 65.5% to produce the same field strength at the rotor's position.

2.2 Prototyping

The designed scanner was prototyped using a combination of 3D printing and planar photolithographic processes similar to the reported process [26]. The housing, alignment adapter,
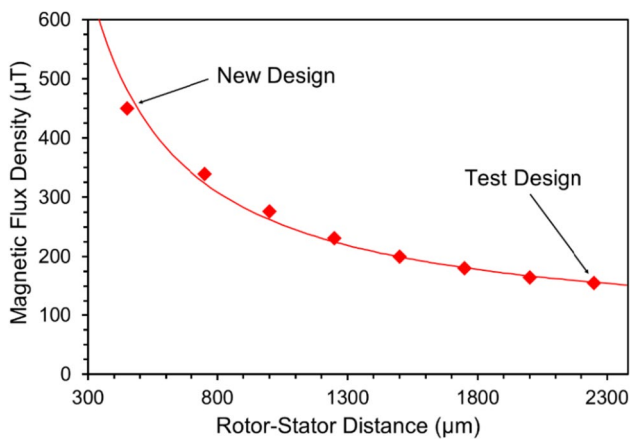
Fig. 3 Simulated magnetic flux density at various distances away from the stator, including the new and test design cases as indicated, in a diagonal configuration at 1 A of the drive current. The trendline shown is hyperbolic ($R^2 = 98.5\%$)

Table 1 Comparisons of simulated magnetic field strength produced in the new and test designs for the diagonal and parallel powering configurations

| Configuration	New design's field strength (µT)	Test design's field strength (µT)	Increase ratio (new/test)
Diagonal	450	155	2.90
Parallel	417	145	2.88

and lighthouse were all fabricated by 3D printing (Form 3 with clear resin v4, Formlabs, MA, USA) that provided a 25-µm printing resolution. After printing, all the parts were washed in isopropyl alcohol and cured at 60 °C for 30 min in the custom curing unit (Form Cure, Formlabs, MA, USA) to harden the resin. The stator was micromachined from double-sided copper-clad polyimide film (Pyralux AP9111R, DuPont, DE, USA; 25-µm-thick polyimide with 35-µm-thick copper). The stator patterns were photolithographically printed onto the top copper layer of the film using a photoresist (AZP4620, MicroChemicals GmbH, Germany) spin-coated on it to serve as a mask for wet etching of the layer (CE-100, Transene, MA, USA). The produced copper pattern then acted as a mask for wet etching of the polyimide substrate in a potassium-hydroxide-based solution to fully pattern the samples of the stator with its four leads, while they were still tied to the bottom copper layer. Wet etching the bottom copper away released the fully constructed individual stator samples. An N50 neodymium ring magnet with an outer diameter (OD) of 1.0 mm and an inner diameter (ID) of 0.5 mm (R0100D-10, SuperMagnetMan, AL, USA) served as the rotor. A type-304 stainless steel tube (0.5-mm OD and 0.3-mm ID) was cut to size and press-fit into the ring magnet to work as the axle. The 3D-printed

lighthouse was then press-fit onto the other side of the axle. Afterward, an aluminum-coated prism mirror with a 0.7-mm size (MPCH-0.7, Tower Optical, FL, USA) was secured into the lighthouse (Fig. 4a).

The actuator was constructed by sandwiching the stator in-between the housing and the alignment adapter. This bent the four stator leads by 90° to run along the outer surfaces of the actuator body (Fig. 4b). The rotor was then placed inside of the housing, and using a 300-µm diameter capillary tube, ~ 1.5 µL of ferrofluid (EFH-1, FerroTec, CA, USA; saturation magnetization 44 mT, viscosity 6 mPa·s) was applied to the magnet rotor to establish the liquid bearing of the actuator, completing the scanner device (Fig. 4c).

2.3 Scanner controller

The scanner was operated with a custom-built drive circuit that used a microcontroller board (Arduino Uno, Arduino, MA, USA) to control the voltage polarity of the microfabricated stator leads (Fig. 5a). Each lead was connected to an inverter circuit built using metal-oxide-semiconductor field-effect transistors (IRFU9024NPBF and IRLU024NPBF, Infineon Technologies AG, Germany) that were controlled by the microcontroller, such that each duration of the eight steps, T_S (in ms), was defined as:
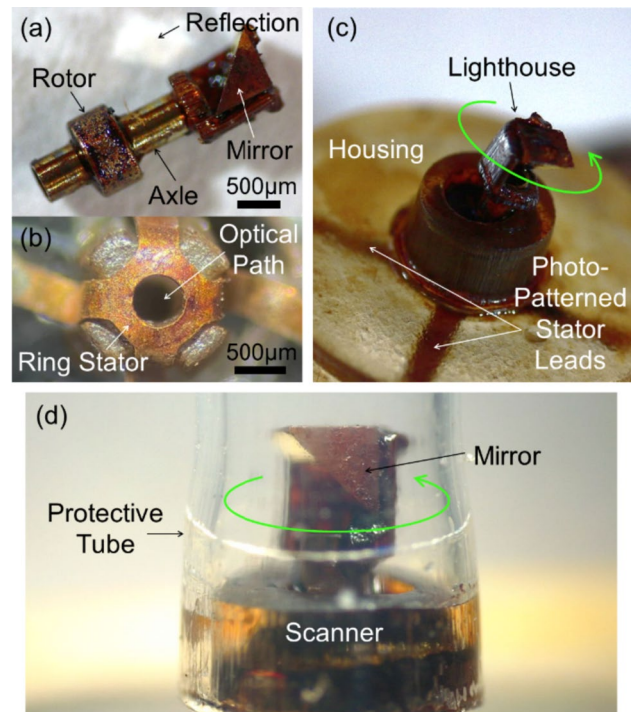
Fig. 4 Samples of prototyped scanner and its structures. **a** The rotor component with the lighthouse and prism mirror. **b** The ring stator with the four leads (bent on a custom base) and optical path. A microfabricated scanner prototype **c** without and **d** with the protective tube
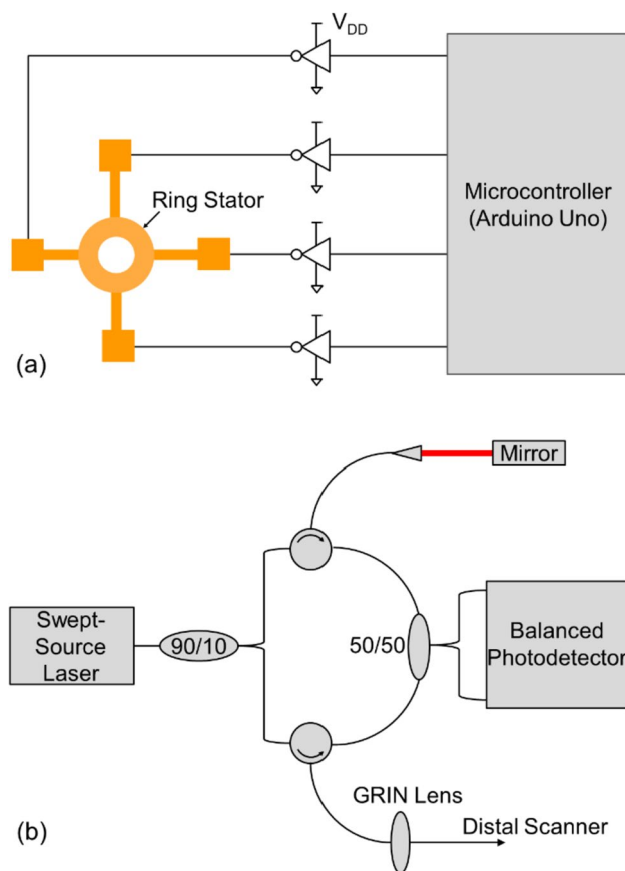
Fig. 5 System schematics. **a** The scanner control circuitry (the external DC supply is indicated as V_{DD}). **b** The OCT system used for test imaging through the developed distal scanner

$$T_S = 1/S_R \times 60 \times 1000/8 = 7500/S_R \qquad (2)$$

where S_R is the rotational speed (in rpm). The total four inverters were powered with an external DC power supply (1902B, BK Precision, CA, USA) that provided the required currents to drive the actuator.

2.4 OCT imaging system and set-up

The OCT system used in the current work is well described elsewhere [24, 27]. Briefly, the system was composed of a fiber-based Mach–Zehnder interferometer driven with a swept-source 1310-nm laser with a 100-nm bandwidth (SSOCT-1310, Axsun Technologies, MA, USA) (Fig. 5b). Spectral interferograms were collected as the laser was periodically swept in wavelength from 1260 to 1360 nm at 50 kHz. The wavelength sweep in the laser is implemented using a high-speed MEMS tunable filter in the laser cavity. The spectral interferograms were detected with a balanced photodetector (PDB420C, Thorlabs, NJ, USA), with the analog waveform being digitized using a high-speed analog–digital converter (ATS9350, AlzarTech,

QC, Canada). The digitizer was k-clocked using the optical k-clock built into the laser such that the signal from the detector was sampled uniformly in k-space. The scan depth was 5 mm (in air) and the optical power delivered by the laser was < 20 mW. The OCT data were then processed and displayed in real time using custom in-house software.

To acquire OCT images, the above laser light was guided through a 125-μm pig-tailed single-mode optical fiber and then focused with a GRIN lens [28] (1.8-mm OD, 3.6-mm working distance, 8° polished face) held inside of a glass ferrule (1.818-mm ID, 2.8-mm OD, 10-mm long). As depicted in Fig. 2a, this ferrule was aligned with the scanner using the 3D-printed adapter, described earlier, to center the OCT imaging beam with the prism mirror. The adapter's hollow core allows for the ferrule to be press-fit in and coupled to the bottom of the actuator housing, centering the GRIN lens with the hollow of the actuator. A protective transparent tube was placed around the scanner to ensure that any object being imaged did not contact with the rotating mirror while allowing the laser beam to pass through the tube without being significantly attenuated. A heat shrinkable tube of fluorinated ethylene propylene (FEP; A1542, Zeus, SC, USA) was used for this purpose, which was thermally shrunk down to have an ID of 2 mm, tightly fitting around the housing (Fig. 4d).

3 Results

3.1 Scanning speeds

To operate the actuator at a specific speed, the stator must draw a minimum current, which is however not always constant for a given speed [29]. Traditional electromagnetic motors characterize this current using a transient response curve, with the current normally surging on the startup and then rapidly falling to a steady state [29]. In light of this, the operation was characterized by recording the two drive currents, the startup and stall currents, where the startup current is the initial current draw required to initiate spinning of the rotor from its stationary state, whereas the stall current is the minimum current required to keep the rotor spinning. The startup current is always greater than the stall current for a variety of reasons, such as static friction being greater than dynamic friction [30]. The startup current was measured by programming the actuator to rotate at a certain speed and then slowly increasing the supplied current until the rotor started to spin. The stall current was then measured by tapering the current down until the rotor stops spinning. All currents above 4 A were pulsed for < 10 s to avoid damaging the drive circuitry. The results showed that there was a distinct difference between the measured startup and stall currents (Fig. 6a), while this was not the case with the test
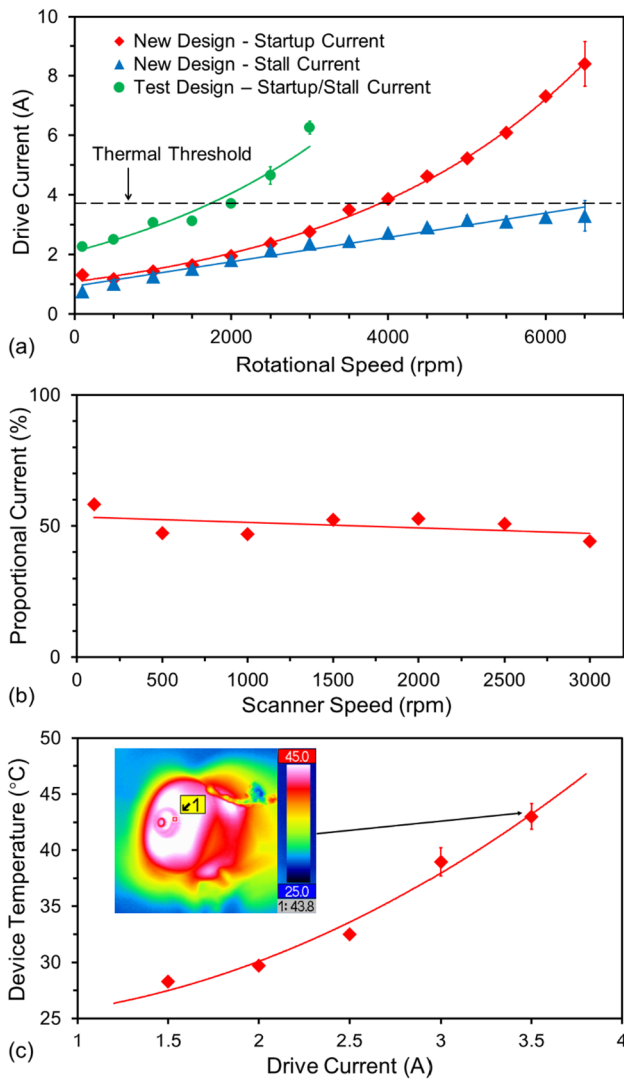
Fig. 6 Electrical and thermal characterizations. **a** Average startup and stall currents of the developed scanner (with error bars of ± standard deviation, SD, measured with five replicate trials) as a function of the rotational speed, shown with the current threshold (3.7 A) equivalent to a biological thermal limit (45 °C; refer to Sect. 3.2); the measured data from the test design [23] also plotted for comparison. **b** The percentage of the new design's (startup) drive current to the test design's drive current as a function of the rotational speed. **c** Average device temperature (with error bars of ± SD, measured with three replicate trials) as a function of the drive current, with the inset showing a captured temperature map of the powered scanner operating at 43.8 °C (measured at the location marked "1" in the map) while operating at 3000 rpm with 3.5 A of drive current; the trendlines is parabolic with an intercept at 25 °C (room temperature) and are well fit (with R^2 of 98.11%)

design that showed no clear difference in terms of these two current modes.

The new actuator required a lower drive current than the test design for a given rotational speed, which was led by the smaller distance between the rotor and stator, as predicted. The simulation result for the new scanner (Table 1)

implies a theoretical maximum reduction of 65.5% in the current consumption from the test design. A comparison of the experimentally measured currents between the two designs (for all scanning speeds up to 3000 rpm, the maximum speed of the test design) shown in Fig. 6b indicated an overall reduction of ~ 50%, slightly less than the simulation result. This deviation could be caused by damping effects (e.g., mechanical friction) associated with the actuation not reflected in the simulation leading to power loss.

3.2 Thermal characterization

The thermal profiles of the previous ferrofluid-based electromagnetic actuators were reported to primarily originate in Joule heating of the stator instead of the friction involved in the ferrofluid bearing [22, 23]. Using a thermal camera (VarioCam HiRes 1.2 M, Jenoptik AG, Germany), temperature behaviors of the new design was characterized for varying drive currents while limiting the maximum temperature to 45 °C, a thermal threshold above which tissue starts to be damaged [31]. The measurement results (Fig. 6c) indicated that the recorded thermal profile was very close to that of the test design [26] and fitted well with a parabolic approximated curve. These are reasonable outcomes because the design of the stator itself was identical to that of the test design, and a similar ferrofluid bearing was used for the present design, i.e., the primary heat source was the drive current (and thus the temperature increase followed a parabolic profile) as also reported with the test design.

3.3 Operation with angled orientations

The actuator design implemented a stopper-cap at the top of the housing, ensuring that the rotor component did not come off as the probe tip is tilted. This practical feature for real use of the probe was verified by spinning a test green laser at 1000 rpm while rotating the entire scanner from upright (0°) to upside down (180°) (Fig. 7). It should be noted that, during this test, there was no change in the required current to spin the rotor, indicating that the scanner was functional with negligible gravitational effects both mechanically and electrically.

3.4 OCT demonstration

The scanner's OCT imaging ability was verified by taking multiple images at both 12.2 Hz (732 rpm) and 24.4 Hz (1464 rpm) using the design and setup described in Sect. 2.4. The human fingers were used as imaging samples for their stratified tissue layers as well as small sweat glands that served as a suitable reference for OCT testing purpose [24, 32]. A pair of an index finger and thumb were firmly pressed around the protective tube of the scanner as it spun the laser

Fig. 7 Tilting test showing the scanner operating at 1000 rpm with a constant current while spinning a green laser at 0, 90, and 180 degrees
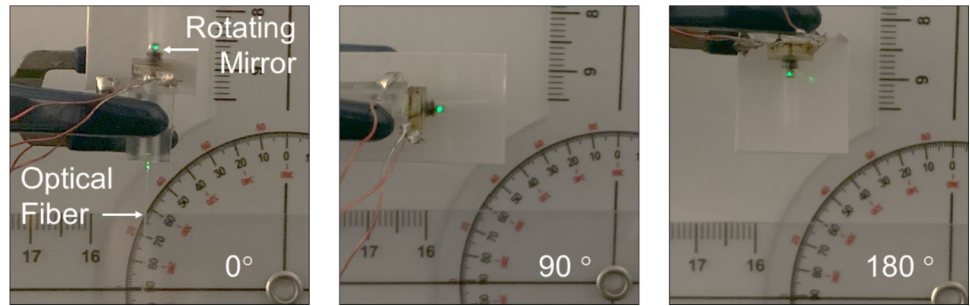
Fig. 8 Examples of the obtained OCT images of an index finger and thumb wrapped around the scanner operating at a scan rate of 12.2 Hz (732 rpm). **a** A wrapped view, demonstrating the scanner's ability of unobstructed 360° imaging. **b** An unwrapped view displaying a layered structure of the live skin tissue including the epidermis, dermis, and sweat gland in the bottom half of the image
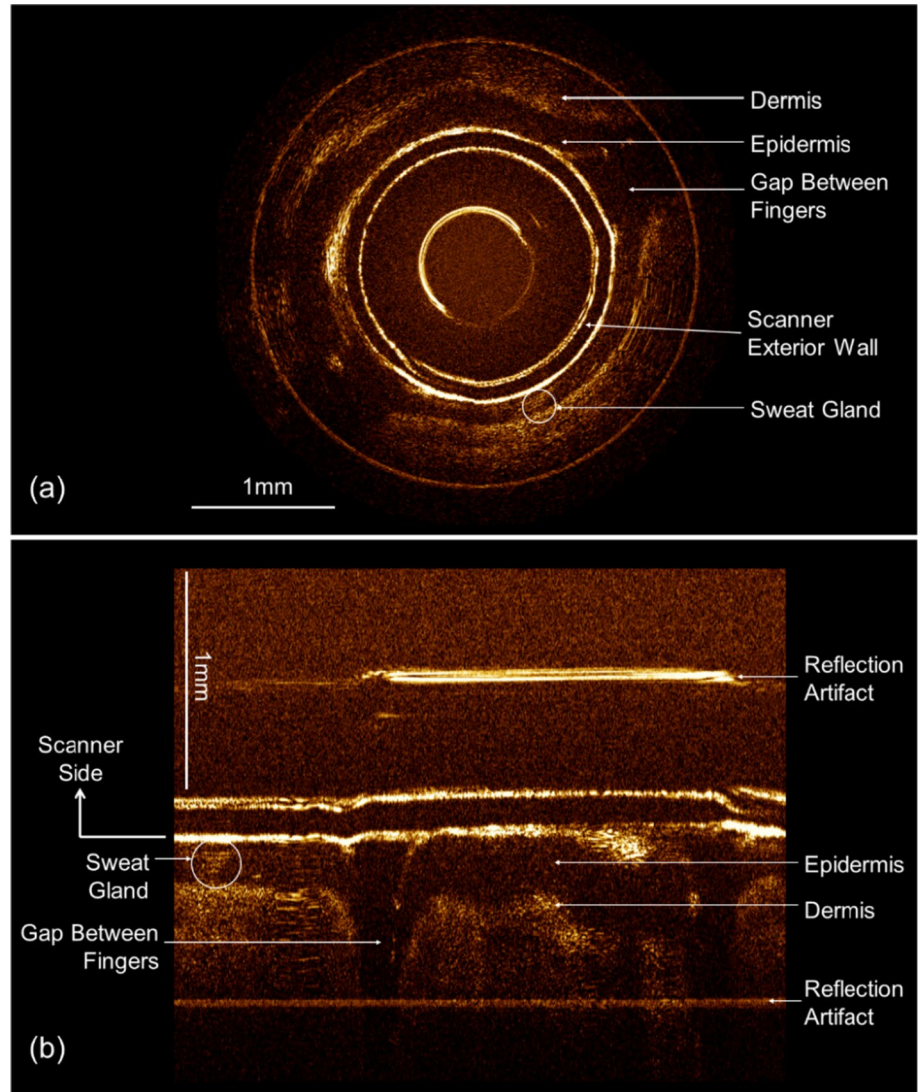
beam. The imaging tests were successfully demonstrated using the particular OCT system described earlier. A sample result from a 12.2-Hz acquisition is shown in Fig. 8, displaying both circular and unwrapped views of the fingers. This demonstration verified the ability for the scanner to differentiate tissue layers (the epidermis vs. the dermis), spot small features (sweat gland), and provide a full 360° view without electrical lead shadows.

4 Discussion

The developed new planar scanner was able to acquire OCT images with no shadows, unachievable with the preceding ferrofluid-based designs [21–24], while being constructed in a smaller form with a 2-mm OD. The scanner's main features are compared with those of reported OCT endoscopic distal scanners with full rotational capabilities in Table 2. When compared to the previous ferrofluid actuator used for OCT imaging [24], the quality and resolution of the obtained OCT images of the finger tissue are comparable, being able to differentiate from the epidermis and dermis, as well as resolve sweat glands. The images acquired using the present scanner are slightly less focused; this was most likely due to the working distance of the GRIN lens not perfectly matching the distance from the lens to the tissue. This can be improved by using an alternative lens with a larger working distance and adding a function to modulate the working distance from the mirror for optimal focus adjustment [33]. Nevertheless, the present scanner still provided an imaging ability sufficient enough to resolve tissue layers and their detailed features.

The prototyped new design was measured to exhibit a noticeable difference between the startup and stall currents above 3000 rpm of the rotation speed (Fig. 6a), a characteristic that the preliminary planar design did not show [26]. This is apparently because the pervious design's maximum speed was 3000 rpm (limited by damaging heat), which was approximately where the startup

and stall currents started to diverge as observed in the new design. While the source of this divergence threshold (~ 3000 rpm) is not fully understood and requires further systematic study, it is speculated to be related to the shear thinning effect of ferrofluid [25]. As the actuator speed rises, the shear thinning effect competes with another phenomenon of ferrofluid where raising the magnetic flux increases its viscosity [25]. This means that increasing the speed causes the two varying factors (increase in shear and increase in magnetic flux) to oppositely affect the ferrofluid's viscosity. This competing relationship could cause an inflection point, such that past it one variable begins to dominate. This might be particularly seen at the above threshold speed level, i.e., while the magnetic flux required to spin the rotor continues to increase the static friction, past that speed the shear-thinning effect could overtake it by lowering the dynamic friction, leading to a difference in the startup and stall currents.

The above feature, representing an improved power efficiency of the new planar design, was revealed to produce a maximum rotation speed of 6500 rpm within the biological thermal threshold (equivalent to 3.7 A of the drive current), which is 3.25 × greater than that of the previous planar design under the same input current. This favorable outcome was brought by the further miniaturization achieved in the new design, which supplied a stronger magnetic flux density to the ferrofluid-suspended rotor (Fig. 3, Table 1) with a drastically narrowed separation between the rotor and stator. The heating effect of the scanner, which limits the scan speed (and therefore OCT performance) for its clinical application, could be improved by fully embedding the actuator within a catheter and providing additional thermal insulation to the surrounding tissue and biofluid. This insulation could allow for even higher scan speeds to be realized while the exterior surface of the catheter stays below the thermal threshold. Another observed phenomenon, which was deteriorated by the heating effect, was a gradual evaporation of the carrier (hydrocarbon) liquid of the ferrofluid used (refer to Sect. 2.2). The reduction of this liquid over time needs to be prevented in order to both maintain the

Table 2 Comparisons of the developed scanner with other distal rotary scanners

Publications	Scanner diameter (mm)	Scanner length (mm)	Max speed (rpm)	Shadow-less 360° view	Actuation type
This work	2	2.8	6500	Yes	Electromagnetic
Test design [26]	2	6	3000	Yes	Electromagnetic
Chen [11]	1.5	10.1	2000	Yes	Ultrasonic
Chang [17]	2.42	~ 12	120	Yes	Piezoelectric
Lee [12]	2.6	~ 7	14,400	No	Electromagnetic
Wang [15]	1.1	~ 2.8	218,400	No	Electromagnetic
Jayhooni [24]	2.25	6	2500	No	Electromagnetic

bearing performance of the ferrofluid and ensure the compatibility of the device for *in-vivo* use. Therefore, future work will look for packaging of the scanner that allows for hermetic sealing of the housing and protective cap in combination with the abovementioned thermal insulation function.

5 Conclusions

This work has prototyped a miniaturized electromagnetic rotary actuator for use as a distal scanner and demonstrated its application to endoscopic OCT. The planar architecture of the actuator design in combination with the self-sustained ferrofluid bearing mechanism enabled the miniaturized implementation of the scanner with higher performance compared with the reported results. The test design that served as a proof-of-concept was improved for integration with an OCT system while significantly reducing the axial size of the scanner, which in turn not only led to notable enhancements of the actuator's power efficiency and maximum speed up to 6500 rpm, but also will raise the distal flexibility of the side-viewing probe. The actuator was successfully operated at any given angle with respect to gravity to verify its essential ability for the endoscope application. The scanner's viability as a high-speed OCT probe was verified by demonstrating imaging of human fingers using a typical OCT system. This imaging test proved that the developed scanner could provide a full 360° field of view without any blind spot in endoscopic OCT. These promising results encourage further development and optimization of this distal scanner for its clinical imaging tests toward realizing an advanced OCT probe.

Declarations

Conflict of interest The authors declare that there is no conflict of interests regarding the publication of this article.

References

1. Zhang J, Nguyen T, Potsaid B, Jayaraman V, Burgner C, Chen S, Li J, Liang K, Cable A, Traverso G, Mashimo H, Fujimoto JG. Multi-MHz MEMS-VCSEL swept-source optical coherence tomography for endoscopic structural and angiographic imaging with miniaturized brushless motor probes. Biomed Opt Express. 2021;12:2384. https://doi.org/10.1364/boe.420394.

2. Fujimoto JG, Pitris C, Boppart SA, Brezinski ME. Optical coherence tomography: an emerging technology for biomedical imaging and optical biopsy. Neoplasia. 2000;2:9–25.

3. Gora MJ, Suter MJ, Tearney GJ, Li X. Endoscopic optical coherence tomography: technologies and clinical applications. Biomed Opt Express. 2017;8:2405. https://doi.org/10.1364/boe.8.002405.

4. Wang TD, van Dam J. Optical biopsy: a new frontier in endoscopic detection and diagnosis. Clin Gastroenterol Hepatol. 2004;2:744–53.

5. Fercher AF, Drexler W, Hitzenberger CK, Lasser T. Optical coherence tomography: principles and applications. Rep Prog Phys. 2003;66:239–303.

6. Tsai TH, Fujimoto J, Mashimo H. Endoscopic optical coherence tomography for clinical gastroenterology. Diagnostics. 2014;4:57–93. https://doi.org/10.3390/diagnostics4020057.

7. Pang Z, Wu J. Miniaturized magnetic-driven scanning probe for endoscopic optical coherence tomography. Biomed Opt Express. 2015;6:2231. https://doi.org/10.1364/boe.6.002231.

8. Kawase Y, Suzuki Y, Ikeno F, Yoneyama R, Hoshino K, Ly HQ, Lau GT, Hayase M, Yeung AC, Hajjar RJ, Jang IK. Comparison of nonuniform rotational distortion between mechanical IVUS and OCT using a phantom model. Ultrasound Med Biol. 2007;33:67–73. https://doi.org/10.1016/j.ultrasmedbio.2006.07.020.

9. Kang W, Wang H, Wang Z, Jenkins MW, Isenberg GA, Chak A, Rollins AM. Motion artifacts associated with in vivo endoscopic OCT images of the esophagus. Opt Express. 2011;19:20722–35. https://doi.org/10.1364/OE.19.020722.

10. Wang T, Pfeiffer T, Regar E, Wieser W, van Beusekom H, Lancee CT, Springeling G, Krabbendam I, van der Steen AFW, Huber R, van Soest G. Heartbeat OCT: in vivo intravascular megahertz-optical coherence tomography. Biomed Opt Express. 2015;6:5021. https://doi.org/10.1364/boe.6.005021.

11. Chen T, Zhang N, Huo T, Wang C, Zheng J, Zhou T, Xue P. Tiny endoscopic optical coherence tomography probe driven by a miniaturized hollow ultrasonic motor. J Biomed Opt. 2013;18:1. https://doi.org/10.1117/1.jbo.18.8.086011.

12. Lee HC, Ahsen OO, Liang K, Wang Z, Cleveland C, Booth L, Potsaid B, Jayaraman V, Cable AE, Mashimo H, Langer R, Traverso G, Fujimoto JG. Circumferential optical coherence tomography angiography imaging of the swine esophagus using a micromotor balloon catheter. Biomed Opt Express. 2016;7:2927–42. https://doi.org/10.1364/boe.7.002927.

13. Liang K, Wang Z, Ahsen OO, Lee HC, Potsaid BM, Jayaraman V, Cable A, Mashimo H, Li X, Fujimoto JG. Cycloid scanning for wide field optical coherence tomography endomicroscopy and angiography in vivo. Optica. 2018;5:36. https://doi.org/10.1364/optica.5.000036.

14. Liang CP, Dong J, Ford T, Reddy R, Hosseiny H, Farrokhi H, Beatty M, Singh K, Osman H, Vuong B, Baldwin G, Grant C, Giddings S, Gora MJ, Rosenberg M, Nishioka N, Tearney G. Optical coherence tomography-guided laser marking with tethered capsule endomicroscopy in unsedated patients. Biomed Opt Express. 2019;10:1207. https://doi.org/10.1364/boe.10.001207.

15. Wang T, Lancée C, Beurskens R, Meijer J, Knapen B, van der Steen AFW, van Soest G. Development of a high-speed synchronous micro motor and its application in intravascular imaging. Sens Actuator A Phys. 2014;218:60–8. https://doi.org/10.1016/j.sna.2014.07.020.

16. Kim KH, Park BH, Maguluri GN, Lee TW, Rogomentich FJ, Bancu MG, Bouma BE, de Boer JF, Bernstein JJ. Two-axis magnetically-driven MEMS scanning catheter for

endoscopic high-speed optical coherence tomography. Opt Express. 2007;15:18130–40. https://doi.org/10.1364/OE.15.018130.

17. Chang S, Murdock E, Mao Y, Flueraru C, Disano J. Stationary-fiber rotary probe with unobstructed 360° view for optical coherence tomography. Opt Lett. 2011;36:4392–4. https://doi.org/10.1364/OL.36.004392.

18. Gorecki C, Bargie S. MEMS scanning mirrors for optical coherence tomography. Photonics. 2021;8:6. https://doi.org/10.3390/photonics8010006.

19. Wang D, Fu L, Wang X, Gong Z, Samuelson SR, Duan C, Jia H, Ma JS, Xie H. Endoscopic swept-source optical coherence tomography based on a two-axis microelectromechanical system mirror. J Biomed Opt. 2013;18:086005. https://doi.org/10.1117/1.JBO.18.8.086005.

20. Luo S, Wang D, Tang J, Zhou L, Duan C, Wang D, Liu H, Zhu Y, Li G, Zhao H, Wu Y, An X, Li X, Liu Y, Huo L, Xie H. Circumferential-scanning endoscopic optical coherence tomography probe based on a circular array of six 2-axis MEMS mirrors. Biomed Opt Express. 2018;9:2104–14. https://doi.org/10.1364/BOE.9.002104.

21. Jayhooni SMH, Assadsangabi B, Takahata K. A stepping micromotor based on ferrofluid bearing for side-viewing microendoscope applications. Sensor Actuator A Phys. 2018;269:258–68. https://doi.org/10.1016/j.sna.2017.11.020.

22. Assadsangabi B, Tee MH, Wu S, Takahata K. Catheter-based microrotary motor enabled by ferrofluid for microendoscope applications. J Microelectromech Syst. 2016;25:542–8. https://doi.org/10.1109/JMEMS.2016.2551222.

23. Assadsangabi B, Jayhooni SMH, Short M, Zeng H, Takahata K. Ferrofluid-enabled micro rotary-linear actuator for endoscopic three-dimensional imaging and spectroscopy. Smart Mater Struct. 2020;29:015025. https://doi.org/10.1088/1361-665X/ab36a0.

24. Jayhooni SMH, Hohert G, Assadsangabi B, Lane PM, Zeng H, Takahata K. A side-viewing endoscopic probe with distal micro rotary scanner for multimodal luminal imaging and analysis. J Microelectromech Syst. 2021;30:433–41. https://doi.org/10.1109/JMEMS.2021.3072617.

25. Rosensweig RE, Neuringer JL. Ferrohydrodynamics. Cambridge University Press; 1985.

26. Searles K, Shalabi N, Jayhooni SMH, Takahata K. A planar micro rotary actuator for endoscopic optical scanning. Sens Actuator A Phys. 2022;345:113768. https://doi.org/10.1016/j.sna.2022.113768.

27. Pahlevaninezhad H, Lee AMD, Hohert G, Lam S, Shaipanich T, Beaudoin EL, MacAulay C, Boudoux C, Lane P. Endoscopic high-resolution autofluorescence imaging and OCT of pulmonary vascular networks. Opt Lett. 2016;41:3209. https://doi.org/10.1364/ol.41.003209.

28. Lee AMD, Hohert G, Angkiriwang PT, MacAulay C, Lane P. Dual-beam manually-actuated distortion-corrected imaging (DMDI) with micromotor catheters. Opt Express. 2017;25:22164. https://doi.org/10.1364/oe.25.022164.

29. Hughes A, Drury B. Electric motors and drives. 5th ed. Newnes; 2019.

30. Martins JAC, Oden JT, Simoes FMF. A study of static and kinetic friction. Int J Eng Sci. 1990;28:29–92. https://doi.org/10.1016/0020-7225(90)90014-A.

31. Ong BB, Milne N, Injury, fatal and nonfatal: Burns and scalds. In: encyclopedia of forensic and legal medicine: 2nd Ed, Elsevier, 2015: pp. 173–181. https://doi.org/10.1016/B978-0-12-800034-2.00220-2.

32. Wurster LM, Shah RN, Placzek F, Kretschmer S, Niederleithner M, Ginner L, Ensher J, Minneman MP, Hoover EE, Zappe H, Drexler W, Leitgeb RA, Ataman C. Endoscopic optical coherence tomography angiography using a forward imaging piezo scanner probe. J Biophotonics. 2019;12:e201800382. https://doi.org/10.1002/jbio.201800382.

33. Duan C, Sun J, Samuelson S, Xie H. Probe alignment and design issues of microelectromechanical system based optical coherence tomography endoscopic imaging. Appl Opt. 2013;52:6589–98. https://doi.org/10.1364/AO.52.006589.